MDPI

Article

One-Pot Au@Pd Dendritic Nanoparticles as Electrocatalysts with Ethanol Oxidation Reaction

Young Su Choi [1,†], Mi-Jung Ji [2,†], Yu Jin Kim [1], Hyeon Jeong Kim [3], Jong Wook Hong [4,*] and Young Wook Lee [1,*]

[1] Department of Education Chemistry and Research Institute of Natural Sciences, Gyeongsang National University, Jinju 52828, Republic of Korea

[2] Carbon Neutral Materials Center, Korea Institute of Ceramic Engineering and Technology, Jinju 52851, Republic of Korea

[3] Department of Chemistry and Research Institute of Natural Sciences, Gyeongsang National University, Jinju 52828, Republic of Korea

[4] Department of Chemistry, University of Ulsan, Ulsan 44610, Republic of Korea

* Correspondence: jwhong@ulsan.ac.kr (J.W.H.); lyw2020@gnu.ac.kr (Y.W.L.)

† These authors contributed equally to this work.

Abstract: The one-pot synthesis strategy of Au@Pd dendrites nanoparticles (Au@Pd DNPs) was simply synthesized in a high-temperature aqueous solution condition where cetyltrimethylammonium chloride (CTAC) acted as a reducing and capping agent at a high temperature. The Au@Pd DNPs with highly monodisperse were shown in high yields by the Au:Pd rate. The nanostructure and optical and crystalline properties of the Au@Pd DNPs were characterized by UV–vis spectroscopy, transmission electron microscopy (TEM), and X-ray diffraction. The Au@Pd DNPs showed an efficient electrochemical catalytic performance rate toward the ethanol oxidation reaction (EOR) due to their nanostructures and Au:Pd rate.

Keywords: CO stripping curve; one-pot synthesis strategy; catalysts of electrocatalytic performance

check for updates

1. Introduction

In the past few decades, nanoparticles (NPs) have attracted attention because of their unique properties and applications [1–5]. In particular, the applications of NPs have been used in various products and reactions, such as fuel cells, portable devices, organic reactions, sensors, and drug delivery [6–11]. In particular, the fuel cells have rapidly increased in fuel cell development using hydrogen, ethylene glycol, methanol, and ethanol as alkaline electrolytes for decades. In addition, the advantage of a direct ethanol fuel cell (DEFC) is that it can produce ethanol in large amounts, it is a renewable energy resource, and it has low toxicity, and this development is increasing due to green energy. The oxidation of ethanol involves twelve electrons per molecule, resulting in higher energy density compared to methanol [12–14]. It has been reported that noble metal NPs have high activity as catalysts for ethanol oxidation reactions [15–18]. Although noble metal NPs are not economically efficient, they are still widely used in fuel cells or photoelectron catalysts because they are easy to control the shape and durability of NPs [15,16]. Noble metal NPs such as Pd, Au, Pt, and Pt have been used due to stability, and the function of the catalysts has been improved by the controlled shape and size of NPs [19–24]. Among various noble metals, Pd is used in fuel cells for formic acid and alcohol oxidation, and it is promising as an eco-friendly energy [25–28]. However, there is a limit to increasing the surface area or energy of Pd NPs. Furthermore, Pd has a disadvantage in that the stability of the catalyst is low due to oxidation reaction [29–31]. To compensate for this, alloy and core–shell structure nanoparticles were synthesized by complementing gold with excellent stability, and it is reported that catalyst stability and reactivity of the catalyst are improved in the fuel

cell reaction [31–34]. In particular, synthesis of the core–shell structure is a method of forming the core first and then the shell through a step reaction, so the experiment method is complicated. Therefore, the method to expand the potential application of core–shell NPs is the development of facile and simple strategic synthesis [35–37].

Here, we report that the one-pot synthesis of bimetallic Au@Pd DNPs is presented. The one-pot synthesis of the Au core and Pd shell was reduced under an aqua solution, and 90 °C temperature conditions resulted in high-yield Au@Pd DNPs. Furthermore, DNPs with controlled branches and muti-arms have been attractive research because of their unique form and enhanced catalytic performance. We measured the electrocatalytic activity of ethanol oxidation with Au@Pd DNPs that controlled the shell by Pd ratio.

2. Experimental Section

Chemicals: Gold (III) choride hydrate ($HAuCl_4$ xH_2O; 99%), Potassium (II) tetra chloride, (K_2PdCl_4; 98%), CTAC (Aldrich, solution in water, 25 wt%) were purchased from Aldrich. Other chemicals, unless specified, were reagent grade, and deionized water with a resistivity of greater than 18.0 MΩ·cm was used in the preparation of aqueous solutions.

Preparation of Nanoparticles

Pd: DNPs: In a typical synthesis of Pd DNs, 0.8 mL of 5 mM aqueous solution of K_2PdCl_4 was added to 5 mL of 30 mM CTAC. The whole system was sealed, heated, and maintained at 90 °C in a conventional forced-convection drying oven for 4 h.

Au@Pd: DNPs: In a typical synthesis Au@Pd DNs, total of 0.8 mL of 5 mM aqueous solution of $HAuCl_4$ and K_2PdCl_4 (Au:Pd 3:5, 1:1, 3:5) were added to 5 mL of 30 mM CTAC. The whole system was sealed, heated, and maintained at 90 °C in a conventional forced-convection drying oven for 4 h.

Au NPs: In a typical synthesis of Au NPs, 0.8 mL of 5 mM aqueous solution of $HAuCl_4$ was added to 5 mL of 30 mM CTAC. The whole system was sealed, heated, and maintained at 90 °C in a conventional forced-convection drying oven for 4 h.

The DNPs and NPs were washed two times with ethanol and deionized water by centrifugation (10,000 rpm for 5 min). In order to confirm the CTAC in the sample before and after centrifugation, sample image and IR were measured to confirm that almost no CTAC remained (Figure S1).

Characterization of nanoparticles: The extinction spectra of Pd, Au@Pd DNPs, and Au NPs were measured by UV-vis absorption spectrometer (SINCO S-3100). TEM images of samples were shown with a TEM (JEOL JEM-2010) operating at 300 kV after placing a drop of hydrosol on carbon-coated Cu grids (200 mesh). For immobilization of Pd, Au@Pd DNPs, and Au NPs, the substrate was washed with triply distilled water and dried. XRD patterns of samples were obtained with a Bruker AXS D8 DISCOVER diffractometer using Cu Kα (0.1542 nm) radiation. The chemical composition surface of the Au@Pd DNPs was indicated by XPS (THERMO Fisher Scientific NEXSA G2 spectrometer), using an Al K X-ray source (1486.6 eV) and a hemispherical electron analyzer. Inductively coupled plasma optical emission spectrometry (ICP-OES, Thermo Fisher Scientific, iCAP PRO XP Duo) were measured amounts of Au and Pd. IR data measured Thermo Scienific (Nicolet summit).

Electrochemical Measurements: Pd, Au@Pd DNPs, and Au NPs were measured by a CH Instruments model 708C potentiostat. Cyclic voltammetry (CV) and chronoamperometry (CA) was used to system of a proper three-electrode cell with counter, reference, and working electrodes of Pt wire, Ag/AgCl (in saturated 3 M KCl), and carbon electrode. Before these catalysts were loaded, the glassy carbon electrode (GCE) was polished with alumina powder and washed thoroughly with Milli-Q water and ethanol. A total of 0.1 M KOH with electrolyte solution were purged with N_2 gas for 30 min. A total of 4 μL of catalyst aqueous solution (metal loading 1 μg: 0.25 mg mL^{-1}) was dropped onto the GCE before CV measurements. After being dried with these products, 4 μL of 0.05 wt% Nafion solution was dropped on these samples, and this was dried in 50 °C oven. After the parched GCE was washed with acetone, water, and ethanol, the product was electrochemically cleaned

by 50 potential cycles at a scan rate of 50 mV s^{-1} form -0.8 to 0.3 V versus Ag/AgCl in an alkaline electrolyte solution (KOH) to eliminate capping agents on the surfaces of catalyst [38]. The ECSA was estimated by the following equation: ECSA = Qo/qo, where Qo is the surface charge that can be obtained from the area under the CV trace of oxygen reduction, and qo is the charge required for reduction of a monolayer of oxygen on the Au and Pd (400 μC/cm^2 and 424 μC/cm^2 ref.: Woods, R. In Electroanalytical Chemistry: A Series of Advances (vol.9); Bard, A. J., Ed.; Marcel Dekker: New York, 1974; pp. 1–162).

3. Results and Discussion

Au@Pd DNPs were prepared from the aqueous solutions of K$_2$PdCl$_4$ and HAuCl$_4$ with CTAC as a reducing agent and surfactant. It has been reported that CTAC, polyvinylpyrroli-done (PVP), and sodium citrate (SC) act as reducing agents and capping agents under high-temperature conditions. The reduction of CTAC reported the presence of a new peak at 1388 cm^{-1} in the CTAC-NPs spectrum that can be assigned to the N=O vibration that indicates the appearance of the nitroso group through the oxidation of CTAC [39]. When synthesizing Pd, Au@Pd DNPs, and Au NPs, the chemical agent of CTAC was used as a bot in order to confirm the nanostructure of DNPs; these were verified through various analyses (Figure S1).

The HAADF-STEM images of Au@Pd DNPs exhibited a dark contrast at the outside of DNPs and a bright contrast at the center of DNPs. HAADF-STEM-EDS mapping images of prepared DNPs indicate that the DNPs had an Au@Pd core–shell structure with a thin Pd shell at the outside surface (Figure 1c,f,i and Figure S2). Furthermore, the Pd shell with lattice spacing in dendrites regions corresponds to the 111 planes of Pd (Figure 1b,e,h). h a reductant and surfactant in 90 °C conditions. The dendritic shell control of Au$_3$@Pd$_5$, Au$_1$@Pd$_1$, and Au$_5$@Pd$_3$ DNPs was possible to synthesize by the Pd ratio. The size of Au$_3$@Pd$_5$, Au$_1$@Pd$_1$, and Au$_5$@Pd$_3$ DNPs measured as edge 35.6 ± 2.3 nm, 40.3 ± 3.2 nm, and 43.3 ± 2.8 nm by TEM images, respectively. When the Au$_3$@Pd$_5$, Au$_1$@Pd$_1$, and Au$_5$@Pd$_3$ DNPs with dendrites of Pd shell were measured by TEM, the shell length of these DNPs were 7.8 ± 1.4, 6.2 ± 1.2, and 5.8 ± 1.1 nm (Figure 1a,d,g). Furthermore, the corresponding fast Fourier transform (FFT) pattern further corroborates the single crystallinity of the Au$_3$@Pd$_5$, Au$_1$@Pd$_1$, and Au$_3$@Pd$_3$ DNPs (Figure S3) [40–42].
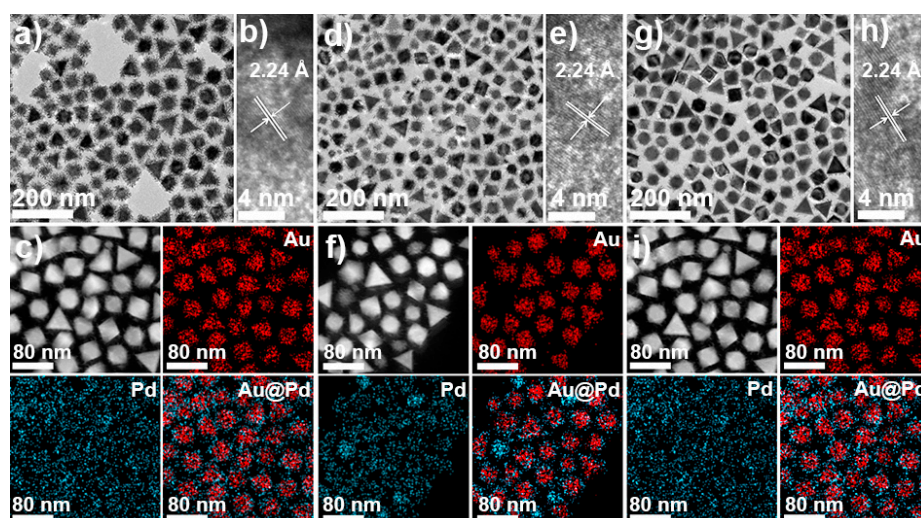
**Figure 1.** TEM, HRTEM and HAADF-STEM image and corresponding EDS elemental mapping images of Au$_3$@Pd$_5$ DNPs (**a–c**), Au$_1$@Pd$_1$ DNPs (**d–f**) and Au$_5$@Pd$_3$ DNPs (**g–i**).

In order to confirm of Au@Pd DNPs structure, Au$_3$@Pd$_5$DNPs represented a core–shell structure by line mapping of HAADF-STEM image and cross-sectional compositional line profiles (Figure S2). When synthesizing only Au and Pd NPs, the shape of Pd NPs had a

dendritic structure, and 2.24 Å of (111) lattice distance plane was confirmed by HRTEM (Figure 2).
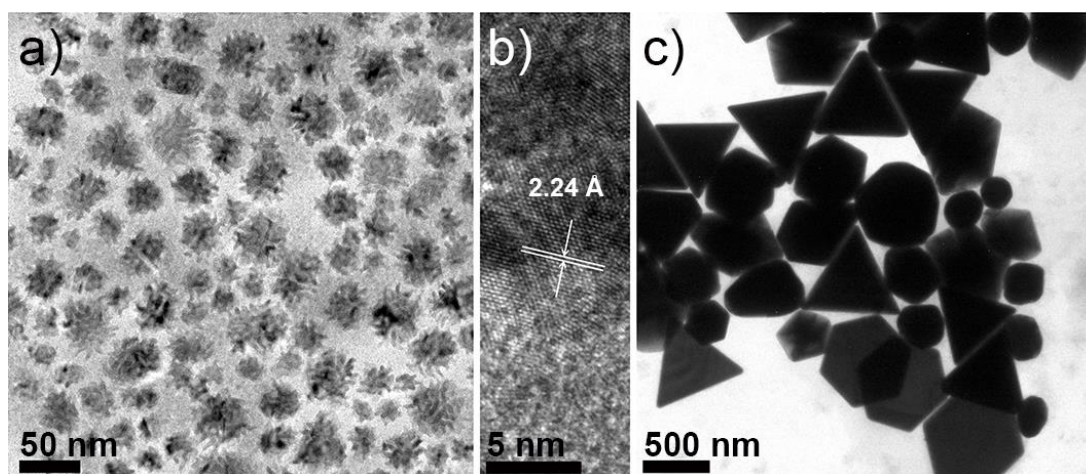
Figure 2. TEM and HR TEM images of (**a**) Pd DNPs, (**b**) Pd DNPs and TEM image of (**c**) Au NPs.

The optical properties of Pd, Au@Pd DNPs, and Au NPs were measured by UV-vis spectroscopy. Figure 3a,c show the images before, and the absence of a peak at 310 and 407 nm correspond to unreduced Au (III) and Pd (II) + CTAC complex, respectively, indicating a complete reduction of metal ions [43]. Figure 3b,d show the post-reaction images and Uv-vis spectra of Au, Pd, and Au@Pd DNPs. In Figure 3, the absorbance at 500–600 nm indicates that the core is Au NPs, and the absorbance of $Au_5@Pd_3$ DNPs increased because the Au ratio increased [44,45]. Au NPs exhibit characteristic surface plasmon adsorption from 600 to 800 nm, while Pd DNPs exhibit overall adsorption with a broad spectrum.
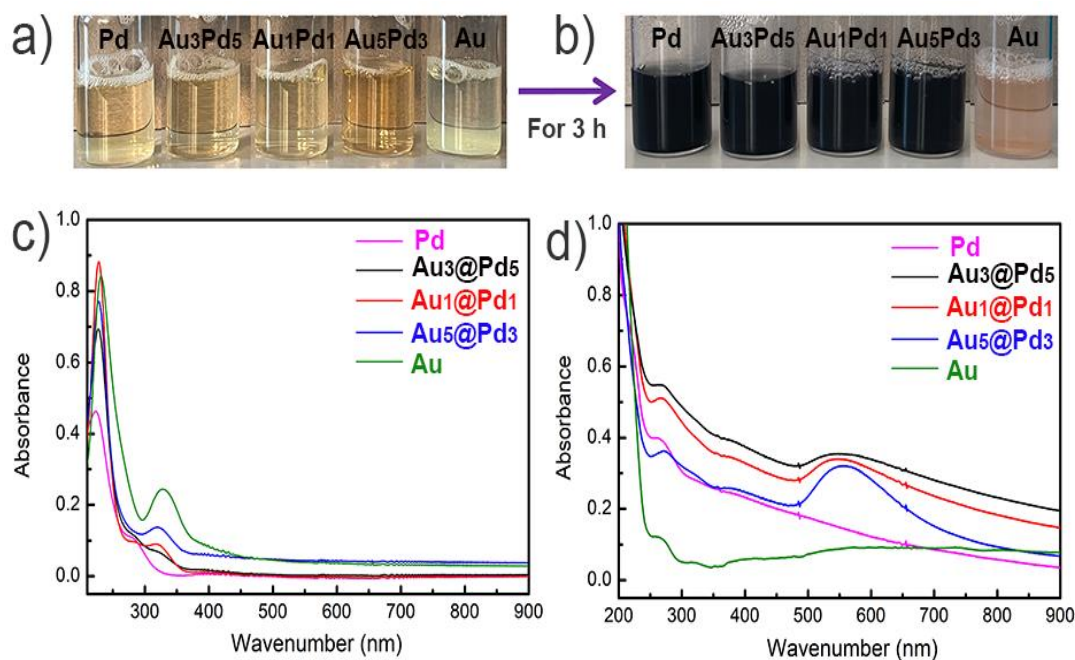

Figure 3. Images and UV-vis spectra in Pd, $Au_3@Pd_5$, $Au_1@Pd_1$, $Au_5@Pd_3$ DNPs and Au NPs of (**a,b**) before reaction and (**c,d**) after reaction.

The behavior of single metal NPs was found to be different from that of the bimetallic core–shell structure. The characteristic absorbance band of Au NPs appearing at

600–800 nm exits at 560 nm because the core–shell NPs have a smaller size than only Au NPs synthesized with Au. UV-vis spectral properties of the Pd, Au@Pd DNPs NPs, and Au NPs have different optical properties depending on their Pd shell thickness, and the size and shape are very different absorbance (Figure 3b).

To confirm the crystalline of their NPs, the X-ray diffraction (XRD) pattern of Pd, $Au_3@Pd_5$, $Au_1@Pd_1$, and $Au_5@Pd_3$ DNPs and Au NPs indicated two diffraction peaks in the range of $30° < 2\theta < 60°$ which can be indexed to diffraction from the (111) and (200) of the face-centered cubic (fcc) structure of metallic Pd and Au@Pd DNPs and Au NPs (Figure 4).
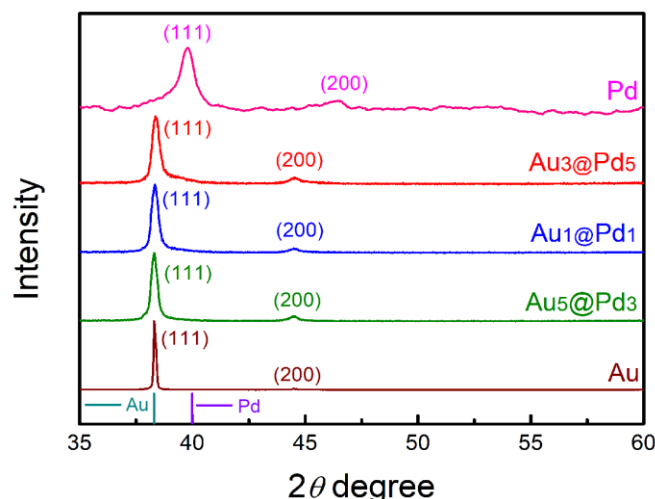

Figure 4. XRD data of Pd, $Au_3@Pd_5$, $Au_1@Pd_1$, $Au_3@Pd_3$ DNPs and Au NPs.

An electrochemical catalyst test was conducted using their NPs with excellent crystallinity. In particular, the electrochemical oxidation reaction of ethanol with Pd-base was chosen as a reaction because of having effective catalytic properties toward ethanol oxidation in alkaline electrolytes and the function of lowering the Pd-CO bonding [45–47]. Therefore, we investigated the electrocatalytic activities of the various prepared Pd, $Au_3@Pd_5$, $Au_1@Pd_1$, $Au_5@Pd_3$ DNPs, and Au NPs in alkaline conditions. The CV profiles present various catalysts in a 0.1 M KOH electrolyte solution with a scan rate = 50 mV s^{-1} (Figure 5a). The current densities of five catalysts were normalized to the electrochemical surface area (ECSA), which was calculated by measuring the Coulombic charge for the reduction of Pd or Au oxide with Pd, $Au_3@Pd_5$, $Au_1@Pd_1$, $Au_5@Pd_3$ DNPs, and Au NPs.

Figure 5a confirms that the shell of Au@Pd DNPs is actually composed of Pd, similar in -0.3 V to the reduction peak position of Pd oxide toward Pd DNPs. Notably, Figure 5b,c indicate specific and mass anodic peaks in the forward and reverse sweeps for the five samples during the ethanol oxidation [48–50]. $Au_3@Pd_5$ DNPs exhibit that the current density of the anodic peak increased outstandingly compared to other catalysts in the forward peak. The ECSA-normalized current densities and the corresponding mass activities of Pd, $Au_3@Pd_5$, $Au_1@Pd_1$, $Au_5@Pd_3$ DNPs and Au NPs in the forward scan (50 mV/s) were 1.21 ± 0.52, 3.59 ± 0.42, 1.41 ± 0.56, 1.36 ± 0.22 and 0.42 ± 0.08 Acm^{-2} and 1365 ± 175, 2268 ± 182, 1493 ± 127, 1452 ± 118, 957 ± 94 and 280 ± 25 mA/mg, respectively (Figure 5b–d). These results indicated that Au@Pd DNPs have been clear to electrocatalytic activity toward ethanol oxidation due to their exposed dendritic Pd amounts as well as Au core. To find the durability of catalysts, we conducted a CA measurement at -0.1 V versus Ag/AgCl, and specific and mass CA curves of Au@Pd DNPs have markedly enhanced stability due to the Au core in a 0.5 M KOH solution containing 0.5 M ethanol (Figure 5d,f). Compared with other reported catalysts, the $Au_3@Pd_5$ DNPs show superiority (Table S1, [51–60]). In general, the electrocatalytic properties in NPs are highly dependent on their geometry and surface electronic structure. In order to investigate the

true role of the core and shell of Au@Pd DNPs in enhancing EOR performance, the catalysts of Pd, Au$_3$@Pd$_5$, Au$_1$@Pd$_1$, Au$_5$@Pd$_3$ DNPs, and Au NPs were investigated by XPS.
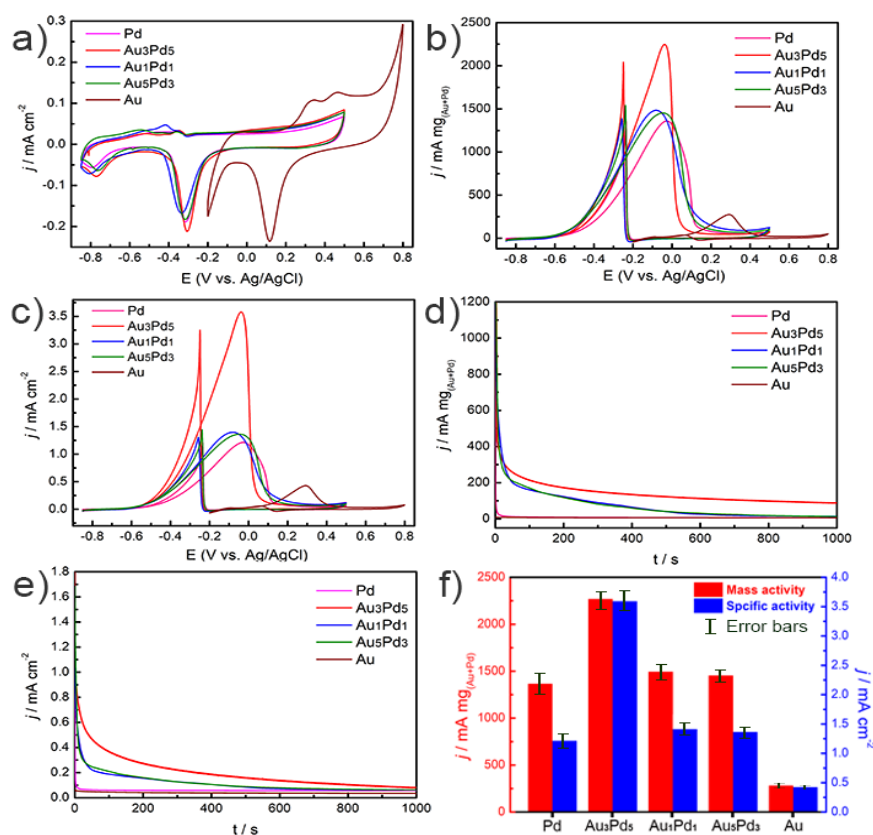
Figure 5. (**a**) CVs obtained with Pd, Au$_3$@Pd$_5$, Au$_1$@Pd$_1$, Au$_3$@Pd$_3$ DNPs and Au NPs. on GCE in 0.1 M KOH were normalized with respect to the ECSA of each catalyst, respectively. Catalytic (**b**) mass and (**c**) specific activities of the different materials in the EOR with 0.1 M KOH + 0.5 M ethanol. (Scan rate = 50 mV/s). CA curves of (**d**) mass activity and (**e**) specific activity obtained with the different catalysts in 0.1 M KOH + 0.5 M ethanol at −0.1 V vs. Ag/AgCl. (**f**) Comparison of EOR mass and specific activities with error bars between the different catalysts.

The high-resolution Au 4f and Pd 3d spectra of all catalysts show two peaks assigned to 4f$_{7/2}$ and 4f$_{5/2}$ in Au, and Pd 3d$_{5/2}$ and 3d$_{3/2}$ in Pd, respectively (Figure 6). The two peaks of the Au@Pd catalysts are shifted to lower binding energies than those of pure Au NPs, indicating an electron transfer from contacted Pd to Au. The shift was induced by the higher electronegativity of Au with 2.54 than Pd with 2.2 [61,62]. The two peaks in Figure 6a represent Pd 3d$_{5/2}$ and 3d$_{3/2}$ trajectories in the high-resolution spectrum. The high-resolution Pd 3d spectra appeared clearly at higher binding energy for the catalysts of Au@Pd DNPs than for the Pd DNPs (Figure 6a). The Au 4f and 3d binding energy of Au@Pd DNPs were lower or higher than Au NPs and Pd DNPs, respectively. As-prepared Au@Pd DNPs and Pd DNPs and Au NPs suggest that both migrations of Au core atom and dissolution of Pd shell atoms induce additional lattice tensile strain in formed Au and Pd. Therefore, the catalytic performance of Au@Pd DNPs in EOR was improved compared to Pd DNPs and Au NPs.

CO anti-poisoning tests were conducted to clarify the Au$_3$@Pd$_5$ DNPs with enhanced EOR performance. In order to clarify the enhanced EOR performance of Au$_1$@Pd$_1$ DNPs, the anti-poisoning test was also performed. CO is widely regarded as an intermediate for EOR, where Pd-based catalysts mimic the adsorption of CH$_3$CO$_{ads}$ [61–63]. We performed CO stripping of the catalyst to confirm the reaction of CO$_{ads}$ and OH$_{ads}$ at the adsorbed interface. Among the products of catalytic decomposition, CO strongly binds with the catalyst at low potentials, blocking the activity of the catalyst.
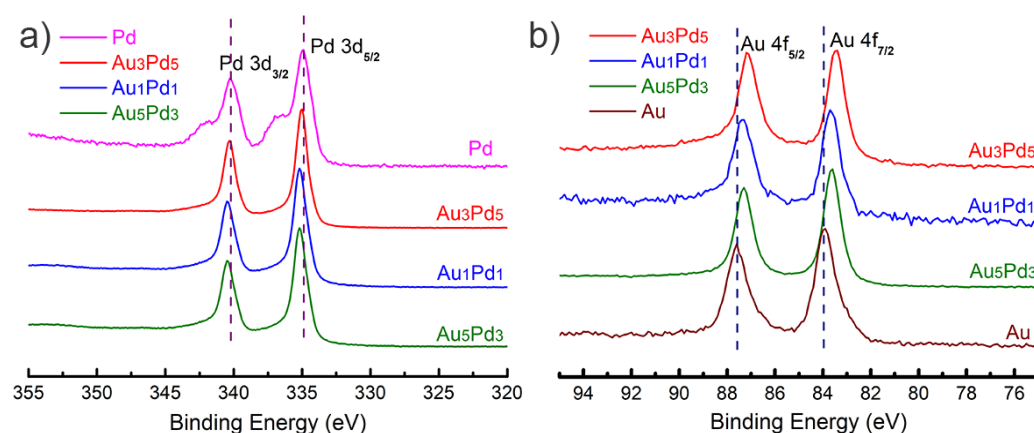
Figure 6. XPS data of (**a**) Pd 3d and (**b**) Au 4f core levels of Pd, $Au_3@Pd_5$, $Au_1@Pd_1$, $Au_3@Pd_3$ DNPs and Au NPs.

We were subjected to CO stripping voltammetry with various catalysts in 0.1 M KOH solution. We adsorbed CO on the metal surface while bubbling it in a one atm electrolyte solution for 20 min. The electrolyte solution was purged with high-purity N_2 to replace CO in the solution and adsorb CO on the Pd surface. The scan rate of 20 mV s^{-1} was performed between −0.8 and 0.3 V to induce CO oxidation of the catalysts. The first voltammetry scan was recorded after CO removal to confirm the removal of CO from Pd. It is possible to improve stability and activity by reducing the strength of CO adsorption through the synergistic effect between Au and Pd. In this regard, the CO stripping test was performed on the CO removal ability of catalysts. Figure 7 shows the voltammetry of various catalysts tested by CO stripping in KOH. Among the various catalysts, $Au_3@Pd_5$ DNPs showed the most negative potential value of −0.120 V and were most effective and indicated the weak peak intensity with the second curve because CO is easily removed. In addition, DNPs with different ratios of $Au_5@Pd_5$ and $Au_7@Pd_3$ DNPs showed more negative potential values than Pd DNPs (Figure 7). Therefore, it was possible to prove the reason for the catalyst of enhanced Au@Pd DNPs in EOR by the CO stripping and XPS binding energy with Au and Pd.
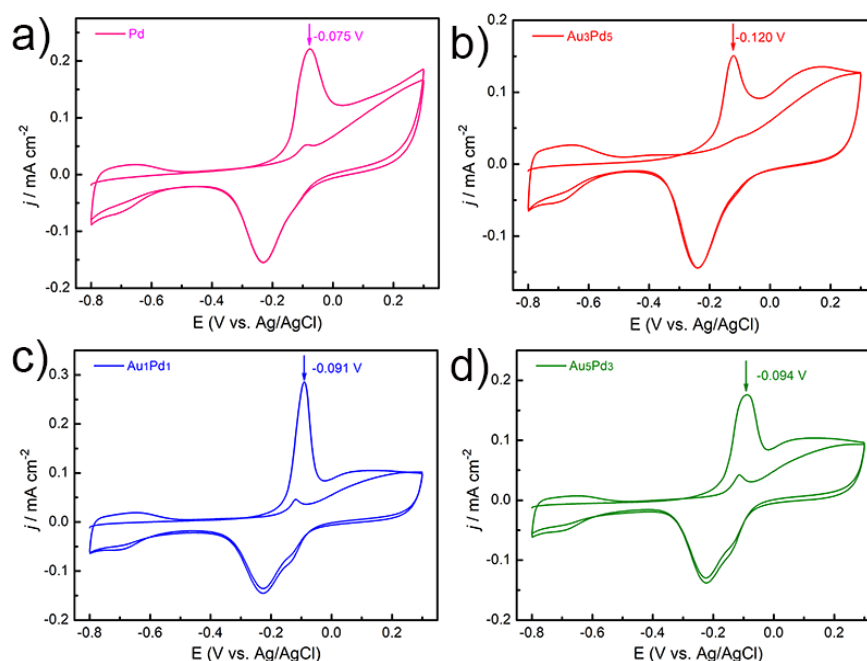
Figure 7. CO stripping curves of various catalysts with (**a**) Pd, (**b**) $Au_3@Pd_5$, (**c**) $Au_1@Pd_1$ and (**d**) $Au_3@Pd_3$ DNPs in 0.1 M KOH at a scan rate of 20 mV/s.

4. Conclusions

In summary, in order to increase the stability of Pd, we synthesized bimetal NPs by adding Au with excellent durability. In addition, we have developed a facile one-pot synthesis of Au@Pd DNPs in an aqua solution that can be easily synthesized in an aqua solution rather than the existing method of core–shell by a step reaction using seed with small nanoparticles.

The morphological and compositional structures of Au@Pd DNPs were dependent on CTAC with reducing agent and surfactant role. Au_3@Pd_5 DNPs showed outstanding electrocatalytic performance toward EOR in alkaline conditions because it was confirmed that they had a weak strength for CO adsorption through CO striping and XPS data. In the future, we expect these catalysts to be widely used for their easy synthesis and application in fuel cells.

Author Contributions: Conceptualization, Y.S.C. and J.W.H.; formal analysis, Y.W.L.; data curation, M.-J.J.; writing—original draft preparation, Y.J.K. and H.J.K.; writing—review and editing J.W.H. and Y.W.L. All authors have read and agreed to the published version of the manuscript.

Institutional Review Board Statement: Not applicable.

Informed Consent Statement: Not applicable.

Data Availability Statement: The data for this work are analyzed in this paper.

Conflicts of Interest: The authors declare no conflict of interest.

References

1. Barbosa, E.C.; Parreira, L.S.; de Freitas, I.C.; Aveiro, L.R.; de Oliveira, D.C.; dos Santos, M.C.; Camargo, P.H. Pt-decorated TiO_2 materials supported on carbon: Increasing activities and stabilities toward the ORR by tuning the Pt loading. *ACS Appl. Energy Mater.* **2019**, *2*, 5759–5768. [CrossRef]
2. Lv, H.; Chen, X.; Xu, D.; Hu, Y.; Zheng, H.; Suib, S.L.; Liu, B. Ultrathin PdPt bimetallic nanowires with enhanced electrocatalytic performance for hydrogen evolution reaction. *Appl. Catal. B Environ.* **2018**, *238*, 525–532. [CrossRef]
3. Hong, J.W.; Kang, S.W.; Choi, B.S.; Kim, D.; Lee, S.B.; Han, S.W. Controlled synthesis of Pd–Pt alloy hollow nanostructures with enhanced catalytic activities for oxygen reduction. *ACS Nano* **2012**, *6*, 2410–2419. [CrossRef] [PubMed]
4. Mirshekari, G.; Rice, C. Effects of support particle size and Pt content on catalytic activity and durability of Pt/TiO_2 catalyst for oxygen reduction reaction in proton exchange membrane fuel cells environment. *J. Power Sources* **2018**, *396*, 606–614. [CrossRef]
5. Huang, W.; Kang, X.; Xu, C.; Zhou, J.; Deng, J.; Li, Y.; Cheng, S. 2D PdAg alloy nanodendrites for enhanced ethanol electroxidation. *Adv. Mater.* **2018**, *30*, 1706962. [CrossRef]
6. Liang, J.; Li, N.; Zhao, Z.; Ma, L.; Wang, X.; Li, S.; Li, Q. Tungsten-Doped L10-PtCo Ultrasmall Nanoparticles as a High-Performance Fuel Cell Cathode. *Angew. Chem. Int. Ed.* **2019**, *58*, 15471–15477. [CrossRef]
7. Zhang, D.; Du, S.; Su, S.; Wang, Y.; Zhang, H. Rapid detection method and portable device based on the photothermal effect of gold nanoparticles. *Biosens. Bioelectron.* **2019**, *123*, 19–24. [CrossRef]
8. Tamura, M.; Kon, K.; Satsuma, A.; Shimizu, K.I. Volcano-curves for dehydrogenation of 2-propanol and hydrogenation of nitrobenzene by SiO_2-supported metal nanoparticles catalysts as described in terms of a d-band model. *ACS Catal.* **2012**, *2*, 1904–1909. [CrossRef]
9. Howes, P.D.; Chandrawati, R.; Stevens, M.M. Colloidal nanoparticles as advanced biological sensors. *Science* **2014**, *346*, 1247390. [CrossRef]

10. Cotí, K.K.; Belowich, M.E.; Liong, M.; Ambrogio, M.W.; Lau, Y.A.; Khatib, H.A.; Stoddart, J.F. Mechanised nanoparticles for drug delivery. *Nanoscale* **2009**, *1*, 16–39. [CrossRef]

11. Quang, N.D.; Majumder, S.; Kim, C.; Kim, D. Incorporation of an Au-rGO layer to enhance the photocatalytic application of optimized CdS thin film. *J. Electrochem. Soc.* **2019**, *166*, H3112. [CrossRef]

12. Lu, Y.; Zhang, J.; Wang, W.; Fan, Y.; Liu, C.; Zhou, J.; Ruan, S. Au-Pd modified SnS$_2$ nanosheets for conductometric detection of xylene gas. *Sens. Actuators B. Chem.* **2022**, *351*, 130907. [CrossRef]

13. de Barros, M.R.; Winiarski, J.P.; Elias, W.C.; de Campos, C.E.M.; Jost, C.L. Au-on-Pd bimetallic nanoparticles applied to the voltammetric determination and monitoring of 4-nitroaniline in environmental samples. *J. Environ. Chem. Eng.* **2021**, *9*, 105821. [CrossRef]

14. Huang, X.; Akdim, O.; Douthwaite, M.; Wang, K.; Zhao, L.; Lewis, R.J.; Hutchings, G.J. Au–Pd separation enhances bimetallic catalysis of alcohol oxidation. *Nature* **2022**, *603*, 271–275. [CrossRef] [PubMed]

15. Huang, X.; He, Z.L.; Chen, Y.; Xu, Q.; Zhu, M.; Zhai, C. Self-standing three-dimensional PdAu nanoflowers for plasma-enhanced photo-electrocatalytic methanol oxidation with a CO-free dominant mechanism. *J. Colloid Interface Sci.* **2022**, *625*, 850–858. [CrossRef]

16. Chen, Y.; Fan, Z.; Luo, Z.; Liu, X.; Lai, Z.; Li, B.; Zhang, H. High-Yield Synthesis of Crystal-Phase-Heterostructured 4H/fcc Au@ Pd Core–Shell Nanorods for Electrocatalytic Ethanol Oxidation. *Adv. Mater.* **2017**, *29*, 1701331. [CrossRef]

17. Liang, W.; Wang, Y.; Zhao, L.; Guo, W.; Li, D.; Qin, W.; Jiang, L. 3D Anisotropic Au@ Pt–Pd Hemispherical Nanostructures as Efficient Electrocatalysts for Methanol, Ethanol, and Formic Acid Oxidation Reaction. *Adv. Mater.* **2021**, *33*, 2100713. [CrossRef]

18. Yu, J.; Jin, H.; Wang, Q.; Wei, X.; Chen, H.; Wang, Y. Coalescence of Au–Pd Nanoropes and their Application as Enhanced Electrocatalysts for the Oxygen Reduction Reaction. *Small* **2022**, *18*, 2203458. [CrossRef]

19. Rodrigues, T.S.; da Silva, A.G.; Camargo, P.H. Nanocatalysis by noble metal nanoparticles: Controlled synthesis for the optimization and understanding of activities. *J. Mater. Chem. A* **2019**, *7*, 5857–5874. [CrossRef]

20. Niu, W.; Zhang, L.; Xu, G. Seed-mediated growth of noble metal nanocrystals: Crystal growth and shape control. *Nanoscale* **2013**, *5*, 3172–3181. [CrossRef]

21. Zhang, W.; Lu, G.; Cui, C.; Liu, Y.; Li, S.; Yan, W.; Huo, F. A family of metal organic frameworks exhibiting size-selective catalysis with encapsulated noble metal nanoparticles. *Adv. Mater.* **2014**, *26*, 4056–4060. [CrossRef] [PubMed]

22. Cai, Y.Y.; Choi, Y.C.; Kagan, C.R. Chemical and Physical Properties of Photonic Noble-Metal Nanomaterials. *Adv. Mater.* **2022**, 2108104. [CrossRef] [PubMed]

23. Takami, A.; Kurita, H.; Koda, S. Laser-induced size reduction of noble metal particles. *J. Phys. Chem. B* **1999**, *103*, 1226–1232. [CrossRef]

24. Chumillas, S.; Busó-Rogero, C.; Solla-Gullón, J.; Vidal-Iglesias, F.J.; Herrero, E.; Feliu, J.M. Size and diffusion effects on the oxidation of formic acid and ethanol on platinum nanoparticles. *Electrochem. Commun.* **2011**, *13*, 1194–1197. [CrossRef]

25. Xue, J.; Han, G.; Ye, W.; Sang, Y.; Li, H.; Guo, P.; Zhao, X.S. Structural regulation of PdCu$_2$ nanoparticles and their electrocatalytic performance for ethanol oxidation. *ACS Appl. Mater. Interfaces* **2016**, *8*, 34497–34505. [CrossRef]

26. Sun, L.; Lv, H.; Feng, J.; Guselnikova, O.; Wang, Y.; Yamauchi, Y.; Liu, B. Noble Metal Based Hollow Mesoporous Nanoparticles: Synthesis Strategies and Application. *Adv. Mater.* **2022**, *34*, 2201954. [CrossRef]

27. Lao, X.; Yang, M.; Chen, J.; Zhang, L.Y.; Guo, P. The ethanol oxidation reaction on bimetallic PdxAg1-x nanosheets in alkaline media and their mechanism study. *Electrochim. Acta* **2021**, *374*, 137912. [CrossRef]

28. Liu, Y.; Wang, D.D.; Zhao, L.; Lin, M.; Sun, H.Z.; Sun, H.C.; Yang, B. Polypyrrole-coated flower-like Pd nanoparticles (Pd NPs@ PPy) with enhanced stability and heat conversion efficiency for cancer photothermal therapy. *RSC Adv.* **2016**, *6*, 15854–15860. [CrossRef]

29. Moreno, M.; Kissell, L.N.; Jasinski, J.B.; Zamborini, F.P. Selectivity and reactivity of alkylamine-and alkanethiolate-stabilized Pd and PdAg nanoparticles for hydrogenation and isomerization of allyl alcohol. *ACS Catal.* **2012**, *2*, 2602–2613. [CrossRef]

30. Li, J.; Zhou, H.; Zhuo, H.; Wei, Z.; Zhuang, G.; Zhong, X.; Wang, J. Oxygen vacancies on TiO$_2$ promoted the activity and stability of supported Pd nanoparticles for the oxygen reduction reaction. *J. Mater. Chem. A* **2018**, *6*, 2264–2272. [CrossRef]

31. Zhu, S.; Qin, X.; Wang, Q.; Li, T.; Tao, R.; Gu, M.; Shao, M. Composition-dependent CO$_2$ electrochemical reduction activity and selectivity on Au–Pd core–shell nanoparticles. *J. Mater. Chem. A* **2018**, *7*, 16954–16961. [CrossRef]

32. Kim, K.; Byun, J.; Kim, H.; Lee, K.S.; Lee, H.S.; Kim, J.; Han, J.W. Systematic Approach to Designing a Highly Efficient Core–Shell Electrocatalyst for N$_2$O Reduction. *ACS Catal.* **2021**, *11*, 15089–15097. [CrossRef]

33. Silva, L.S.; Almeida, C.V.; Meneses, C.T.; Batista, E.A.; Santos, S.F.; Eguiluz, K.I.; Salazar-Banda, G.R. AuPd/C core–shell and alloy nanoparticles with enhanced catalytic activity toward the electro-oxidation of ethanol in alkaline media. *Appl. Catal. B.* **2019**, *251*, 313–325. [CrossRef]

34. Wang, L.; Yamauchi, Y. Autoprogrammed synthesis of triple-layered Au@ Pd@ Pt core–shell nanoparticles consisting of a Au@ Pd bimetallic core and nanoporous Pt shell. *J. Am. Chem. Soc.* **2010**, *132*, 13636–13638. [CrossRef] [PubMed]

35. Chen, H.; Li, Y.; Zang, F.; Zhang, G.; Fan, X. Graphene supported Au-Pd bimetallic nanoparticles with core-shell structures and superior peroxidase-like activities. *J. Mater. Chem.* **2011**, *21*, 17658–17661. [CrossRef]

36. Tsuji, M.; Ikedo, K.; Matsunaga, M.; Uto, K. Epitaxial growth of Au@ Pd core–shell nanocrystals prepared using a PVP-assisted polyol reduction method. *CrystEngComm* **2012**, *14*, 3411–3423. [CrossRef]

37. Lee, Y.W.; Im, M.; Hong, J.W.; Han, S.W. Dendritic ternary alloy nanocrystals for enhanced electrocatalytic oxidation reactions. *ACS Appl. Mater. Interfaces* **2017**, *9*, 44018–44026.

38. Lee, S.; Cho, H.; Kim, H.J.; Hong, J.W.; Lee, Y.W. Shape-and Size-Controlled Palladium Nanocrystals and Their Electrocatalytic Properties in the Oxidation of Ethanol. *Materials* **2021**, *14*, 2970. [CrossRef]

39. Lee, Y.W.; Kim, M.; Kim, Y.; Kang, S.W.; Lee, J.H.; Han, S.W. Synthesis and electrocatalytic activity of Au–Pd alloy nanodendrites for ethanol oxidation. *J. Phys. Chem. C.* **2010**, *114*, 7689–7693. [CrossRef]

40. Lee, Y.W.; Kim, M.; Kang, S.W.; Han, S.W. Polyhedral bimetallic alloy nanocrystals exclusively bound by {110} facets: Au–Pd rhombic dodecahedra. *Angew. Chem. Int. Ed.* **2011**, *50*, 3466–3470. [CrossRef]

41. Metin, Ö.; Sun, X.; Sun, S. Monodisperse gold–palladium alloy nanoparticles and their composition-controlled catalysis in formic acid dehydrogenation under mild conditions. *Nanoscale* **2013**, *5*, 910–912. [CrossRef] [PubMed]

42. Lee, Y.W.; Kim, M.; Kim, Z.H.; Han, S.W. One-step synthesis of Au@ Pd core–shell nanooctahedron. *J. Am. Chem. Soc.* **2009**, *131*, 17036–17037. [CrossRef] [PubMed]

43. Chiu, C.Y.; Yang, M.Y.; Lin, F.C.; Huang, J.S.; Huang, M.H. Facile synthesis of Au–Pd core–shell nanocrystals with systematic shape evolution and tunable size for plasmonic property examination. *Nanoscale* **2014**, *6*, 7656–7665. [CrossRef] [PubMed]

44. Ferrer, D.; Torres-Castro, A.; Gao, X.; Sepulveda-Guzman, S.; Ortiz-Mendez, U.; Jose-Yacaman, M. Three-layer core/shell structure in Au–Pd bimetallic nanoparticles. *Nano Lett.* **2007**, *7*, 1701–1705. [CrossRef]

45. Chen, Y.; Wang, H.; Liu, C.J.; Zeng, Z.; Zhang, H.; Zhou, C.; Yang, Y. Formation of monometallic Au and Pd and bimetallic Au–Pd nanoparticles confined in mesopores via Ar glow-discharge plasma reduction and their catalytic applications in aerobic oxidation of benzyl alcohol. *J. Catal.* **2012**, *289*, 105–117. [CrossRef]

46. Ahmed, M.S.; Jeon, S. Electrochemical activity evaluation of chemically damaged carbon nanotube with palladium nanoparticles for ethanol oxidation. *J. Power Sources* **2015**, *282*, 479–488. [CrossRef]

47. Huang, W.; Ma, X.Y.; Wang, H.; Feng, R.; Zhou, J.; Duchesne, P.N.; Li, Y. Promoting effect of Ni(OH)$_2$ on palladium nanocrystals leads to greatly improved operation durability for electrocatalytic ethanol oxidation in alkaline solution. *Adv. Mater.* **2017**, *29*, 1703057. [CrossRef]

48. Zhou, X.; Ma, Y.; Ge, Y.; Zhu, S.; Cui, Y.; Chen, B.; Zhang, H. Preparation of Au@ Pd Core–Shell Nanorods with fcc-2H-fcc Heterophase for Highly Efficient Electrocatalytic Alcohol Oxidation. *J. Am. Chem. Soc.* **2021**, *144*, 547–555. [CrossRef]

49. Wu, C.; Li, H.; He, H.; Song, Y.; Bi, C.; Du, W.; Xia, H. Compressive strain in core–shell Au–Pd nanoparticles introduced by lateral confinement of deformation twinnings to enhance the oxidation reduction reaction performance. *ACS Appl. Mater. Interfaces* **2019**, *11*, 46902–46911. [CrossRef]

50. Zhang, H.; Luo, Y.; Chen, D.; Liu, H.; Cui, P.; Yang, J. Ionic liquid-derived core–shell gold@ palladium nanoparticles with tiny sizes for highly efficient electrooxidation of ethanol. *Green Energy Environ.* **2021**, *6*, 229–235. [CrossRef]

51. Zhu, C.; Guo, S.; Dong, S. PdM (M = Pt, Au) bimetallic alloy nanowires with enhanced electrocatalytic activity for electro-oxidation of small molecules. *Adv. Mater.* **2012**, *24*, 2326–2331. [CrossRef] [PubMed]

52. Jiang, R.; Tran, D.T.; McClure, J.P.; Chu, D. A class of (Pd–Ni–P) electrocatalysts for the ethanol oxidation reaction in alkaline media. *ACS Catal.* **2014**, *4*, 2577–2586. [CrossRef]

53. Qiu, X.; Dai, Y.; Tang, Y.; Lu, T.; Wei, S.; Chen, Y. One-pot synthesis of gold–palladium@ palladium core–shell nanoflowers as efficient electrocatalyst for ethanol electrooxidation. *J. Power Sources* **2015**, *278*, 430–435. [CrossRef]

54. Zhang, L.F.; Zhong, S.L.; Xu, A.W. Highly branched concave Au/Pd bimetallic nanocrystals with superior electrocatalytic activity and highly efficient SERS enhancement. *Angew. Chem. In. Ed.* **2013**, *52*, 645–649. [CrossRef]

55. Wang, L.; Liu, Z.; Zhang, S.; Li, M.; Zhang, Y.; Li, Z.; Tang, Z. In situ assembly of ultrafine AuPd nanowires as efficient electrocatalysts for ethanol electroxidation. *Int. J. Hydrogen Energy* **2021**, *46*, 8549–8556. [CrossRef]

56. Yang, Y.; Jin, L.; Liu, B.; Kerns, P.; He, J. Direct growth of ultrasmall bimetallic AuPd nanoparticles supported on nitrided carbon towards ethanol electrooxidation. *Electrochim. Acta* **2018**, *269*, 441–451. [CrossRef]

57. Zhang, G.; Liu, Z.; Xiao, Z.; Huang, J.; Li, Q.; Wang, Y.; Sun, D. Ni$_2$P-graphite nanoplatelets supported Au–Pd core–shell nanoparticles with superior electrochemical properties. *J. Phys. Chem. C* **2015**, *119*, 10469–10477. [CrossRef]

58. Cai, K.; Liao, Y.; Zhang, H.; Liu, J.; Lu, Z.; Huang, Z.; Han, H. Controlled synthesis of Au-island-covered Pd nanotubes with abundant heterojunction interfaces for enhanced electrooxidation of alcohol. *ACS Appl. Mater. Interfaces* **2016**, *8*, 12792–12797. [CrossRef] [PubMed]

59. Wang, W.; Zhang, J.; Yang, S.; Ding, B.; Song, X. Au@ Pd core–shell nanobricks with concave structures and their catalysis of ethanol oxidation. *ChemSusChem* **2013**, *6*, 1945–1951. [CrossRef]

60. Caglar, A.; Kivrak, H. Highly active carbon nanotube supported PdAu alloy catalysts for ethanol electrooxidation in alkaline environment. *Int. J. Hydrogen Energy* **2019**, *44*, 11734–11743. [CrossRef]

61. Su, Y.; Li, C.; Xu, L.; Xue, J.; Yuan, W.; Yao, C.; Hou, S. Palladium nanoparticles supported on flower-like boron, nitrogen doped carbon for electrochemical oxidation ethanol reaction. *J. Alloys Compd.* **2022**, *901*, 163333. [CrossRef]

62. Liu, Y.; Li, W.; Zhao, G.; Qin, G.; Li, Y.; Liu, Y. Self-driven microstructural evolution of Au@ Pd core–shell nanoparticles for greatly enhanced catalytic performance during methanol electrooxidation. *Nanoscale* **2021**, *13*, 3528–3542. [CrossRef] [PubMed]

63. Hernández, A.R.; Estrada, E.A.; Ezeta, A.; Manríquez, M.E. Formic acid oxidation on AuPd core-shell electrocatalysts: Effect of surface electronic structure. *Electrochim. Acta* **2019**, *327*, 134977. [CrossRef]